Quaternion analysis of beam multi-type vibration data for damage detection

First published: **01 Feb 2022**

which has been published in final form at

https://onlinelibrary.wiley.com/doi/10.1002/stc.2867

Quaternion Analysis of Beam Multi-type Vibration Data for Damage Detection

Mohsen Mousavi[a,b], Damien Holloway*[a], J.C. Olivier[a], Amir H. Gandomi*[b]

[a] *School of Engineering, University of Tasmania, Hobart 7005, Tasmania, Australia*
[b] *Faculty of Engineering and IT, University of Technology Sydney, Ultimo, NSW 2007, Australia*

Abstract

In this paper two damage sensitive features (DSF), one baseline dependent (DSF_1) and the other one baseline free (DSF_2), are proposed based on the Quaternion analysis of the phase trajectory of a beam vibration due to a moving mass. To that end, new Quaternions are constructed with the displacement, velocity and acceleration of the beam mid-span as the elements of the Quaternion vectors. The new DSFs are obtained based on the concept of the angular velocity of a curve in 3D space characterised by a Quaternion. For the baseline dependent case, the proposed DSF_1 needs to be calculated for both intact and damaged beam subjected to the same experiment, whereas in the baseline free case DSF_2 data from only the damaged beam are sufficient for damage detection. The performance of the proposed DSFs is compared against another technique introduced in the literature through several examples and Monte Carlo simulations. Both road roughness and 10% measurement noise effects are taken into account in performance evaluation of the proposed DSFs. The results show that the proposed DSFs are more successful in locating damage on a simply supported beam.

Keywords: `Moving Load, Vibration, Damage Detection, Quaternion Analysis, Angular Velocity, Phase Trajectory`

2010 MSC: 00-01, 99-00

Email addresses: `Corresponding authors:` `damien.holloway@utas.edu.au` (Damien Holloway*), `gandomi@uts.edu.au` (Amir H. Gandomi*)

1. Introduction

In a review of bridge damage identification techniques conducted by An *et al.* bridge structures are classified into beam, truss, arch, cable-stayed or suspension models [1]. The present work will focus on beam-type bridges.

Different structural health monitoring techniques have been proposed for damage detection of beam type bridge structures. One method is to study the vibration of the bridge subjected to a moving mass [2, 3]. The main advantage is that the properties of the applied force such as magnitude and velocity can readily be controlled [4, 5]. Thus, a moving mass (such as a vehicle model) is passed across the beam (bridge model) and vibration data are sampled at some points on the beam. Different damage detection strategies can then be used to estimate location and severity of damage.

New damage sensitive features (DSF) for structural damage detection have been proposed during the past decade [6], deploying new signal processing techniques such as Empirical Mode Decomposition (EMD) [7] and Variational Mode Decomposition (VMD) [8]. Methods based on these techniques attempt to detect a peak or change in the recorded vibration data as an indication of damage when the mass traverses the defective area on the bridge [9]. Among all the signal processing techniques, time domain techniques have been of interest recently. The most commonly used methods for bridge damage detection includes wavelet transform [10, 11] and EMD [12, 13, 14, 15, 16]. These techniques do not rely on any finite element model/analysis of the intact bridge as they study only the vibration data measured from the damaged structure. However, more often than not a baseline needs to be constructed from the vibration data obtained from the intact bridge subjected to the same experiment (the same magnitude of the mass with the same velocity) [4, 16, 17].

It has been shown that the response of the beam subjected to a quasi-static moving load can be divided into two components: (1) a part corresponding only to the velocity of the moving load and independent of any inertia properties, referred as the static component, and (2) a part containing the bridge natural frequency responses and referred to as the dynamic component [18]. As such, the structural health monitoring of bridge structures is mostly related to study of the above parts either individually or together. The abovementioned signal decomposition algorithms may be used to separate the static and dynamic parts. For instance, EMD decomposes a non-stationary non-linear signal into its constructive intrinsic mode functions (IMF).

It is known that the higher frequency IMFs following EMD normally correspond to the dynamic response, and are more sensitive to an abrupt change of stiffness, that is, crack damage [13]. Accordingly, Roveri *et al.* exploited EMD to separate the dynamic part of the deflection time history of a simply supported beam subjected to a moving load and showed that the instantaneous frequency (IF) of the first IMF (highest frequency component) of the vibration response shows a peak at the time instant when the load moves over the defective area on the beam [12]. However, the authors did not consider the road profile effects on damage detection. Recently, OBrien *et al.* used the first IMF of the decomposed acceleration data of a beam subjected to a moving load with road roughness effects included [16]. The authors then introduced a DSF based on the difference between the signals obtained from the intact and damaged structure, suggesting that this subtraction can remove the effect of the road profile excitation. He and Zhu separated the time varying frequency component of a beam subjected to a moving load from its total dynamic response using a multi-scale discrete wavelet transform (DWT) for damage localisation [11].

As far as exploiting the static part of the beam vibration data is concerned, it has been shown that a small moving load velocity is best used. As such, these techniques exploit a quasi-static moving load passing over the bridge to derive only the semi-static response of the beam. The Maxwell-Betti principle of reciprocal deflection can be invoked to show that the response at some point A on a beam subjected to a quasi-static load is equal to the deflection profile of the whole beam when a static force is applied at A. This property has been recently used by Sun *et al.* to obtain the curvature of the beam [18]. Yang *et al.* also showed that the curvature of the beam is sensitive to damage and therefore can be considered a good damage indicator [19]. He *et al.* similarly argue that the response of the bridge structure subjected to a quasi-static moving vehicle is approximately equal to its displacement influence line (DIL) [4]. Therefore, they introduce a damage index based on the the area encircled by the DIL change. He *et al.* argued that the static component of the response of the beam subjected

to a moving load is preferred in damage localisation. As such, the authors used a multi-scale discrete wavelet transform to separate the moving frequency component for damage localisation [11].

Recently, Zhang *et al.* introduced a technique that exploits multi-type vibration measurements to construct the phase trajectory of the vibration of the beam at some points on the beam [17]. In the proposed technique, it is assumed that the phase trajectory of the intact structure subjected to a similar moving load is available. Therefore, the Euclidean distance between these two curves after using a low-pass filter is used for damage localisation. Despite conducting an experimental study, the authors did not include the road roughness profile excitation effects in their simulations.

The present paper exploits the idea of the multi-type vibration measurement proposed in [17] to construct the phase trajectory of the beam mid-span vibration due to a moving mass. The road profile excitation has been taken into account in all the simulations in this paper. Further, although Yang and Lin suggested that the vehicle mass can be neglected compared to the mass of the bridge, in this paper, the interaction between the mass and the bridge is also considered [20]. Accordingly, two new DSFs, namely DSF_1 and DSF_2, based on a Quaternion analysis of the phase trajectory of the intact and damaged beam are proposed, where DSF_1 and DSF_2 are respectively baseline dependent baseline free damage sensitive features.

2. Vehicle bridge interaction (VBI) simulation considering road roughness

2.1. Bridge and vehicle models

In this section, a finite element model of the vehicle bridge interaction is presented for the purpose of simulations (Figure 1). The vibration of a simply supported beam subjected to a moving mass has been studied by several researchers [21, 22, 23] and the following model is based on these.

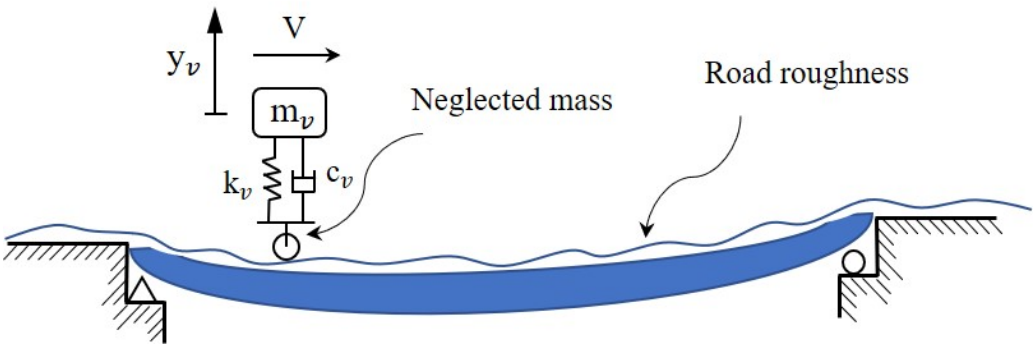

Figure 1: Moving load with suspension system over a bridge with rough surface.

Hermite cubic shape functions for beam elements are used for the finite element model as follows,

$$\begin{aligned} N_1 &= 1 - 3\zeta^2 + 2\zeta^3 \\ N_2 &= L_e\left(\zeta - 2\zeta^2 + \zeta^3\right) \\ N_3 &= 3\zeta^2 - 2\zeta^3 \\ N_4 &= L_e\left(-\zeta^2 + \zeta^3\right). \end{aligned} \tag{1}$$

From these, the cubic Hermitian interpolation vector $[N]_c$ evaluated at the contact point is constructed and used in the model of the bridge-vehicle interaction as follows,

$$\begin{aligned} &\begin{bmatrix} m_v & 0 \\ 0 & [m_b] \end{bmatrix} \begin{Bmatrix} \ddot{y}_v \\ \{\ddot{q}_b\} \end{Bmatrix} + \begin{bmatrix} c_v & -c_v\{N\}_c^\tau \\ -c_v\{N\}_c & [c_b] + c_v\{N\}_c\{N\}_c^\tau \end{bmatrix} \begin{Bmatrix} \dot{y}_v \\ \{\dot{q}_b\} \end{Bmatrix} \\ &+ \begin{bmatrix} k_v & -c_v V\{N'\}_c^\tau - k_v\{N\}_c^\tau \\ -k_v\{N\}_c & [k_b] + c_v V\{N\}_c\{N'\}_c^\tau + k_v\{N\}_c\{N\}_c^\tau \end{bmatrix} \begin{Bmatrix} y_v \\ \{q_b\} \end{Bmatrix} \\ &= \begin{Bmatrix} c_v V r_c' + k_v r_c \\ -c_v V r_c'\{N\}_c - k_v r_c\{N\}_c - m_v g\{N\}_c \end{Bmatrix}, \end{aligned} \tag{2}$$

where $[m_b]$, $[c_b]$, and $[k_b]$ represent respectively the mass, damping and stiffness matrices of the finite element model of the beam. The model also includes a vehicle mass m_v traversing the beam at a constant velocity, sprung with stiffness k_v and damping ratio ζ_v, through which interaction between the mass and the beam is considered. The vertical displacements of the moving mass and the nodal degrees of freedom (vertical translations and rotations) of the beam elements are denoted by y_v and $\{q_b\}$ denote respectively. Note that in Equation 2, τ and $'$ represent respectively the transpose of a matrix and its derivative with respect to the position.

Finally, r_c in Equation 2 is an artificial road roughness generated by the following equation presented in [24] based on ISO 8608,

$$r_c(x_R) = \sum_{i=0}^{N} 2^k \times 10^{-3} \times \sqrt{\Delta n} \left(\frac{n_0}{i\Delta n}\right) \cos\left(2\pi i \Delta n x_R + \phi_i\right), \tag{3}$$

where the constant $(2^k \times 10^{-3})$ has units $\mathrm{m}^{3/2}$ and Δn has units m^{-1}, hence r_c has units m. The constant scalar k depends on the ISO road profile classification and takes an integer value from 3 to 9, corresponding to the profiles from class A to class H, and $n_0 = 0.1\ \mathrm{m}^{-1}$. Also in Equation 3, x_R denotes the variable abscissa on the road with respect to the reference point, ϕ_i is a random phase angle within the range of 0 to 2π with a uniform probabilistic distribution, and $N = L/B$ and $\Delta n = 1/L$, where L is the length of the road profile and B is the wavelength of the shortest spatial component of the roughness profile.

2.2. Bridge and vehicle properties

Quantity	**Nomenculture**	**Value**
Beam length	L	35 m
Beam cross-section height	h	2 m
Beam cross-section width	w	1 m
Beam density	ρ	2500 kg/m^3
Beam modulus of elasticity	E	32.5 GPa
Beam damping ratio	ζ_b	5%
Vehicle mass	m_v	1000 kg
Vehicle suspension stiffness	k_v	45 kN
Vehicle suspension damping	ζ_v	10%
Vehicle velocity	V	5 m/s
Sampling frequency	S_f	100 Hz

Table 1: VBI simulation model scalars.

The beam geometrical and mechanical properties are identical to the example studied in [25] and are shown in the top half of Table 1, while vehicle and suspension properties are shown in the lower half. Note that the behaviour is governed primarily by the first mode natural frequency, and that other combinations of properties achieving the same natural frequency will produce similar beam responses. The vehicle mass is taken to be 1000 kg, and according to [26] an optimised suspension stiffness is within the range 41–45 kN/m, hence in this paper a value of 45 kN/m is used.

Rayleigh damping models i.e. of the form $[c] = \alpha[m] + \beta[k]$, are considered for the beam and suspension. The Rayleigh constants α and β were set to achieve the target damping ratios at the first two natural frequencies as specified in Table 1, namely 5% for the beam at the first two beam-alone natural frequencies, and 10% for the suspension system.

In this paper a class A ($k = 3$ in Equation 3) road roughness profile is considered. In order to achieve a reasonable initial condition at the start of the transverse of the mass across the bridge it is assumed that the mass has been moving over the rough road for a distance equal to the length of the bridge L before it arrives at the left hand side of the bridge, then continues moving over the bridge until it reaches the right hand side. Therefore, a road profile for a length of $2L$ is generated and used

in simulations. The simulated road roughness is shown in Figure 2 which is almost 100 times greater in magnitude than the one considered in [25].

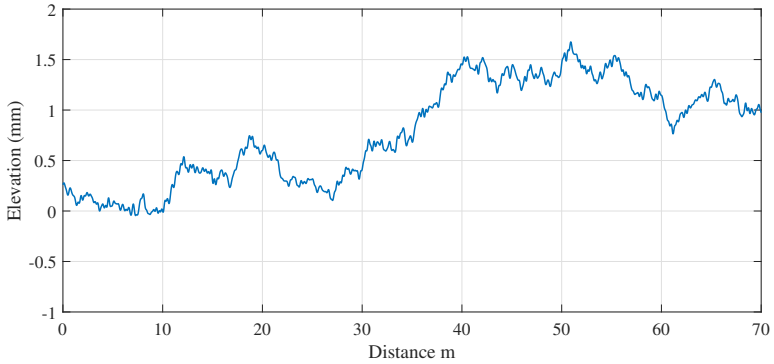

Figure 2: Road profile used in sumulations, starting one beam length ($L_b = 35$ m) before the left end of the beam and ending at the right end of the beam. The beam spans from 35 m to 70 m.

2.3. Modeling the crack

Damage is now introduced as a zero-length spring located between two standard beam elements, with rotational and translational stiffnesses of k_r and k_t, respectively [27, 28]. The stiffness matrix of the crack element is thus

$$k_d = \begin{bmatrix} k_t & 0 & -k_t & 0 \\ 0 & k_r & 0 & -k_r \\ -k_t & 0 & k_t & 0 \\ 0 & -k_r & 0 & k_r \end{bmatrix}. \tag{4}$$

By choosing k_r and k_t sufficiently large, the two section of the beam are fully connected and damage does not exist. Since usually only the loss of rotational stiffness is considered (representing an open crack) k_t is taken here to be a large value of 10^{20} N/m, while k_r follows the model proposed in [29],

$$k_r = \left[\frac{2h}{EI} \left(\frac{\alpha}{1-\alpha} \right)^2 \left(5.93 - 19.69\alpha + 37.14\alpha^2 - 35.84\alpha^3 + 13.12\alpha^4 \right) \right]^{-1}, \tag{5}$$

in which $\alpha = 0$ represents no damage ($k_r = \infty$) and $\alpha = 1$ indicates a completely defective section ($k_r = 0$).

2.4. Equation solution

The beam is assumed to be simply supported and is divided into 35 beam elements with rotational and translational degrees of freedom at each node, as shown in Figure 3. Note that the crack elements are not shown in this figure, and that the relevant nodes need to be duplicated.

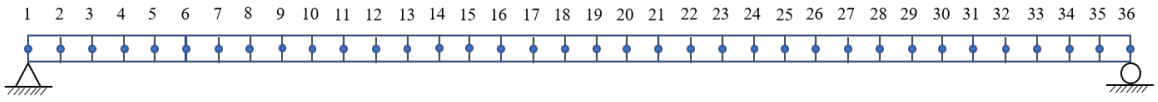

Figure 3: The beam is divided into 35 beam elements bounded by the nodes shown.

Equation 2, is solved using Newmark constant average acceleration method with $\beta = 0.25$ and $\gamma = 0.5$ via MATLAB.

Similar to [17], the phase trajectory of the vibration of the beam approximately at its mid-span (node 18, i.e. 17 m from the beam left support) will be used for damage detection in this paper. As such, the displacement $x(t)$, velocity $v(t)$ and acceleration $a(t)$ of the beam at its midspan are required. Figure 4 shows such a phase trajectory for the example of this paper (without the inclusion of road roughness effects) constructed from these multi-type measurements.

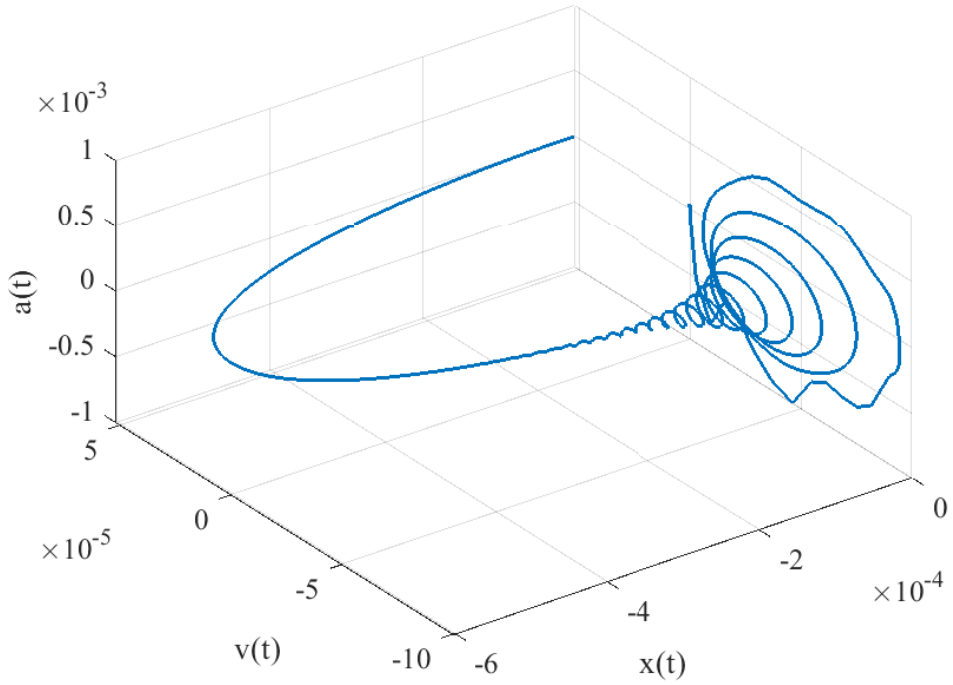

Figure 4: Phase trajectory of the intact beam without road roughness subjected to a moving mass at its mid-span.

3. Some basics of Quaternions

In order to keep the paper self-contained some basics of Quaternion arithmetic and calculus are explained in this section.

It was the great mathematician W. R. Hamilton who proposed the idea of Quaternions in 1844 [30]. A Quaternion is defined as the sum of a scalar q_0 and a vector q as follows,

$$q = q_0 + \boldsymbol{q} = q_0 + q_1\,\hat{\boldsymbol{i}} + q_2\,\hat{\boldsymbol{j}} + q_3\,\hat{\boldsymbol{k}} \tag{6}$$

where $\hat{\boldsymbol{i}} = (1,0,0)$, $\hat{\boldsymbol{j}} = (0,1,0)$, and $\hat{\boldsymbol{k}} = (0,0,1)$ with the following fundamental rules,

$$\begin{aligned} \hat{\boldsymbol{i}}^2 = \hat{\boldsymbol{j}}^2 = \hat{\boldsymbol{k}}^2 = \hat{\boldsymbol{i}}\hat{\boldsymbol{j}}\hat{\boldsymbol{k}} &= -1 \\ \hat{\boldsymbol{i}}\hat{\boldsymbol{j}} = -\hat{\boldsymbol{j}}\hat{\boldsymbol{i}} &= \hat{\boldsymbol{k}} \\ \hat{\boldsymbol{j}}\hat{\boldsymbol{k}} = -\hat{\boldsymbol{k}}\hat{\boldsymbol{j}} &= \hat{\boldsymbol{i}} \\ \hat{\boldsymbol{i}}\hat{\boldsymbol{k}} = -\hat{\boldsymbol{k}}\hat{\boldsymbol{i}} &= \hat{\boldsymbol{j}}. \end{aligned} \tag{7}$$

The norm of the Quaternion q, therefore, is defined as $||q|| = \sqrt{q_0^2 + q_1^2 + q_2^2 + q_3^2}$ from which one can obtain the unit Quaternion as $\frac{q}{||q||}$.

Given the formulae 7, it is easy to show that the product of two Quaternions $p = p_0 + \boldsymbol{p}$ and $q = q_0 + \boldsymbol{q}$ is obtained as follows,

$$p \otimes q = p_0\,q_0 - \boldsymbol{p}\,.\,\boldsymbol{q} + p_0\,\boldsymbol{q} + q_0\,\boldsymbol{p} + \boldsymbol{p} \times \boldsymbol{q} \tag{8}$$

where in Equation 8, "." and "$\times$" denote respectively vector inner and cross products. The conjugate of the Quaternion q is denoted q^* and defined as

$$q^* = q_0 - \boldsymbol{q}\,, \tag{9}$$

where it can be shown that,

$$q \otimes q^* = q^* \otimes q = ||q||^2\,. \tag{10}$$

Assuming that Q is the set of all Quaternions, then $\forall\ p,\ q,\ r\ \in\ Q$ the following are some of the properties of Quaternion multiplication,

$$p \otimes q \neq q \otimes p \text{ in general} \tag{11}$$
$$(p \otimes q)\ \otimes\ r = p \otimes (q\ \otimes\ r) \tag{12}$$
$$p \otimes (q + r) = p \otimes q + p \otimes r \tag{13}$$
$$1 = 1 + 1\,\hat{\mathbf{i}} + 1\,\hat{\mathbf{j}} + 1\,\hat{\mathbf{k}} \tag{14}$$
$$1 \otimes q = q \otimes 1 = q \tag{15}$$
$$\text{if } q \neq 0 \implies \exists\, q^{-1} \in Q \implies q \otimes q^{-1} = q^{-1} \otimes q = 1 \tag{16}$$
$$(q\ \otimes\ p)^* = p^* \otimes q^* \tag{17}$$

Assuming that $q(t) = q_0(t) + \boldsymbol{q}(t)$ is a time dependent Quaternion, then its time derivative is equal to $\dot{q} = \dot{q_0} + \dot{\boldsymbol{q}}$ and can be obtained as follows,

$$\dot{q} = \lim_{\Delta t \to 0} \frac{q(t + \Delta t) - q(t)}{\Delta t}\,. \tag{18}$$

In this paper the concept of angular velocity is used. For this, we proceed with two theorems and one definition,

Theorem 1. *Let $q(t)$ be a time dependent unit Quaternion function. The derivative of $q(t)$ can be obtained using the following formula in which $\omega(t)$ is the angular velocity of the Quaternion at time t.*

$$\dot{q}(t) = \frac{1}{2}\,\omega(t) \otimes q(t) \tag{19}$$

A formal proof of the above theorem can be found in [31].

Right multiplying the both sides of the Equation 19 by q^* and keeping in mind that $qq^* = ||q||^2 = 1$ for a unit Quaternion, one can obtain an equation for the time dependent angular velocity as follows,

$$\omega(t) = 2\,\dot{q}(t) \otimes q^*(t)\,. \tag{20}$$

Note that Equation 20 applies only if q is a unit Quaternion.

Definition 3.1. *A vector in $\mathbb{R}^3$ is defined as a pure Quaternion.*

Theorem 2. *Angular velocity $\omega(t)$ corresponding to the unit Quaternion $q(t)$ is a pure Quaternion itself.*

Proof. From Equation 10 we have $q(t) \otimes q^*(t) = 1$ for a unit Quaternion, and therefore its derivative is

$$\frac{d}{dt}(q(t) \otimes q^*(t)) = \dot{q}(t) \otimes q^*(t) + q(t) \otimes \dot{q}^*(t) = 0, \tag{21}$$

hence

$$\dot{q}(t) \otimes q^*(t) \;=\; -q(t) \otimes \dot{q}^*(t) \tag{22}$$
$$\;=\; -(\dot{q}(t) \otimes q^*(t))^* \tag{23}$$

by property 17. In other words (from Equation 20)

$$\omega(t) = -\omega^*(t) \tag{24}$$

and Equation 9 implies that the constant part of this must be equal to zero, i.e. that $\omega(t)$ is a pure Quaternion.

■

4. Proposed damage sensitive features (DSF)

4.1. A baseline dependent damage sensitive feature (DSF_1)

In order to define DSF_1, first a Quaternion is defined based on the phase trajectory of the vibration of the beam mid-span. Consider a time dependent Quaternion $q(t) = t + \bar{a}(t)\,\hat{\boldsymbol{i}} + \bar{v}(t)\,\hat{\boldsymbol{j}} + \bar{x}(t)\,\hat{\boldsymbol{k}}$ in which t is time and

$$\begin{aligned}\bar{x}(t) &= \frac{x(t)}{\max(x(t)) - \min(x(t))}\\ \bar{v}(t) &= \frac{v(t)}{\max(v(t)) - \min(v(t))}\\ \bar{a}(t) &= \frac{a(t)}{\max(a(t)) - \min(a(t))}\,.\end{aligned} \tag{25}$$

We now construct

$$p(t) = 2\,\dot{q}(t) \otimes q^*(t). \tag{26}$$

Note that this is similar to the expression for angular velocity for a unit Quaternion, Equation 20, though since q is not a unit Quaternion, $p(t)$ contains a scalar component due to the changing magnitude of q. Expanding according to Equation 8, and using the subscript '0' to denote the scalar part of this[1],

$$p_0 = 2(\dot{q}_0 q_0 + \dot{\boldsymbol{q}} \cdot \boldsymbol{q}) = 2(t^2 + \bar{x}\bar{v} + \bar{v}\bar{a} + \bar{a}\dot{\bar{a}}), \tag{27}$$

we define

$$\mathrm{DSF}_1(t) = p_0^{(d)}(t) - p_0^{(h)}(t) \tag{28}$$

where $p_0^{(h)}(t)$ and $p_0^{(d)}(t)$ are obtained from the healthy (intact) and damaged beams respectively.

The performance of DSF_1 is studied through Monte Carlo simulations and the results are compared to a damage sensitive feature proposed in [17] in sections to follow.

4.1.1. Numerical results and discussions using DSF_1

In this section, two different damage scenarios are studied, denoted D1 and D2 and defined in Table 2. In scenario D1 a crack is present at 10 m from the left support, while in D2 two cracks are present at 10 and 29 m relative to the left support (equivalent to normalised times 0.2857 and 0.8286), with damage severity α of 0.3 and 0.2, respectively.

Table 2: Damage scenarios, damage location is measured from the left support.

Damage scenario	**Damage location (m)**	**Damage severity α**
D1	10	0.3
D2	10, 29	0.3, 0.2

It is assumed in all cases that the measurements (displacement, acceleration, and velocity) at the beam mid-span are contaminated by 10% noise, simulated in accordance with [4] as

$$\hat{\delta} = \delta + \frac{\kappa}{100} n_{\text{noise}}\ \sigma(\delta), \tag{29}$$

where δ denotes the noise-free vector with standard deviation $\sigma(\delta)$, κ denotes the noise level (10 in this case), n_{noise} denotes a vector with the same length as δ of random independent variables following a standard normal distribution, and $\hat{\delta}$ represents the simulated vector of noisy measurement.

4.1.2. Signal preconditioning

Prior to computing the value of the damage sensitive features the simulated noisy intact and damaged signals were pre-processed to remove noise in two ways:

[1] One could write $q_0 = \frac{1}{2}(q + q^*)$ for any Quaternion q to obtain the scalar part.

1. Using a robust discretised spline based MATLAB code, based on a technique proposed in [32]. The technique seeks to minimise the following goal function to balance the fidelity in data:

$$F(\hat{y}) = ||\hat{y} - y||^2 + sP(\hat{y}) \tag{30}$$

in which, y and $\hat{y}$ are respectively the original and smoothed signals, s is a smoothing parameter, a real positive scalar that controls the degree of smoothing, and $P(\hat{y})$ is a penalty term that reflects the roughness of the smoothed data.
2. Using a low-pass filter, as performed in [17], with a cutoff frequency of 3 Hz, which is slightly higher than the first natural frequency of the beam (2.68 Hz).

4.1.3. Benchmark detection method

After signal preconditioning, results of damage detection using DSF_1 were compared against a method described in [17] also based on the $(\bar{x}, \bar{v}, \bar{a})$ vector. The method of [17] uses the Euclidean distance between normalised spatial coordinates of the damaged and intact beam trajectory at each time instant as a damage sensitive feature, DI, given by

$$\text{DI}(t) = \sqrt{(\bar{x}_d(t) - \bar{x}_h(t))^2 + (\bar{v}_d(t) - \bar{v}_h(t))^2 + (\bar{a}_d(t) - \bar{a}_h(t))^2}. \tag{31}$$

Here again the subscripts h and d correspond to the healthy and damaged cases respectively.

4.1.4. Damage detection using baseline dependent DSF_1 with smoothing

Let us first consider the scenario D1. Figure 5 compares the phase trajectories of the mid-span beam vibration for the intact beam and damage scenario D1 when a moving mass is traversing the beam with velocity 1 m/s. The effect of the road roughness profile shown in Figure 2 is included in all sub-figures. The signal is first shown in Figure 5a without any additional signal noise, while Figure 5b shows the same signal contaminated by 10% noise. Two different smoothing parameters are applied in order to study the effect of smoothing intensity on damage detection, namely $s = 1000$ and $s = 10000$, as can be seen respectively in Figures 5c and 5d.

The scalar parts of the of $p^{(h)}(t)$ and $p^{(d)}(t)$ are shown in Figure 6. As can be seen from the figures it is not possible to distinguish the effect of damage visually. However, subtracting the intact case from its damaged counterpart to obtain DSF_1 will reveal the location of the damage, as is evident from Figures 7a and 7c. Figures 7b and 7d compare the damage detection for the same cases using DI as given in Equation 6a, based on [17]. In the less aggressive smoothing case ($s = 1000$) both DSF_1 and DI appear noisy, and it is hard to conclusively distinguish the location of the damage without any prior knowledge. A further observation is that a large fluctuation in DI is evident in all simulations at the beginning of the experiment, but this fluctuation is not present in the proposed DSF_1. This phenomenon addresses one of the main advantages of the proposed DSF_1.

More aggressive smoothing ($s = 10000$) is now applied to mitigate both of these effects in DSF_1 and DI, as evident in Figures 7d and 7c. Therefore, $s = 10000$ is chosen as a better candidate for damage detection in what follows.

Next, the maximum values of both DSF_1 and DI are sought and proposed as damage locations. We see that both DSF_1 and DI are successful in damage localisation, but it is not possible to reliably evaluate their performance by only observing a single simulation. Moreover, it is also not clear how to distinguish a damaged case from an undamaged one.

One of the advantages of numerical methods in damage detection, is that they can be used easily in Monte Carlo simulations for better evaluation of methods [33]. Hence, a Monte Carlo simulation strategy is now used, where the signals obtained from both intact and damaged beams subjected to the moving mass are contaminated with 10% noise for 1000 different random realizations, and statistical distributions of maximum DSF_1 and DI are calculated in order to determine both the ability of detection and the likelihood of false alarms.

Using the results of the Monte Carlo simulations and assuming that both DSF_1 and DI reach a peak at the location of the crack, a histogram of the maximum values is shown for DSF_1 and DI in Figures 8a and 8b. These figures show that the proposed DSF_1 is more successful in separating the

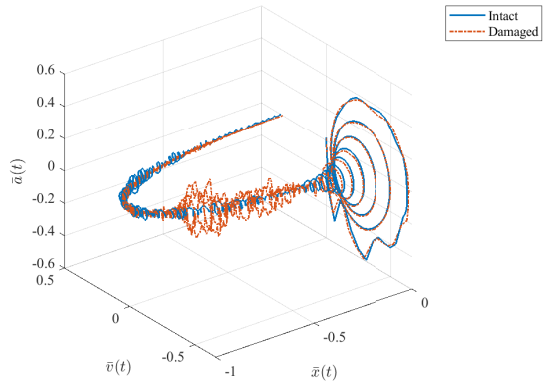

(a) Noiseless trajectories

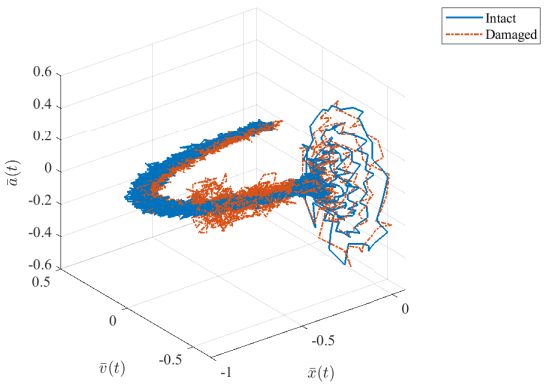

(b) Noisy trajectories

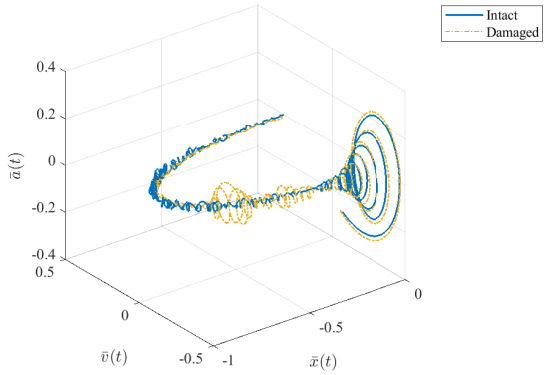

(c) Smoothed trajectories ($s = 1000$)

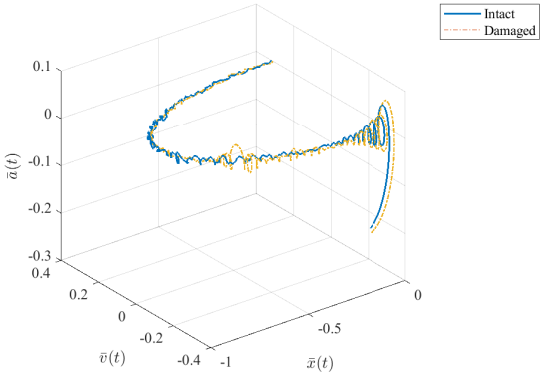

(d) Smoothed trajectories ($s = 10000$)

Figure 5: Phase trajectories of the intact and damaged beam subjected to a moving mass at its mid-span considering the road roughness effect, (a) noiseless, (b) noisy, (c) smoothed ($s = 1000$), and (d) smoothed ($s = 10000$).

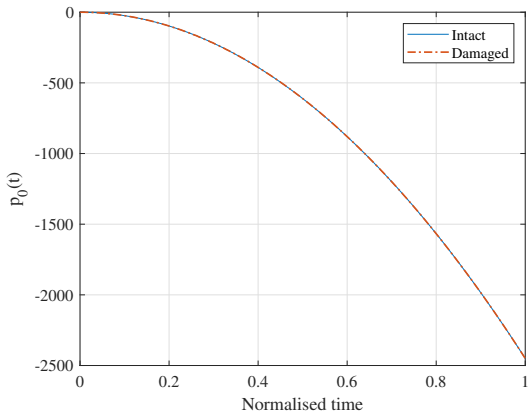

(a) $s = 1000$

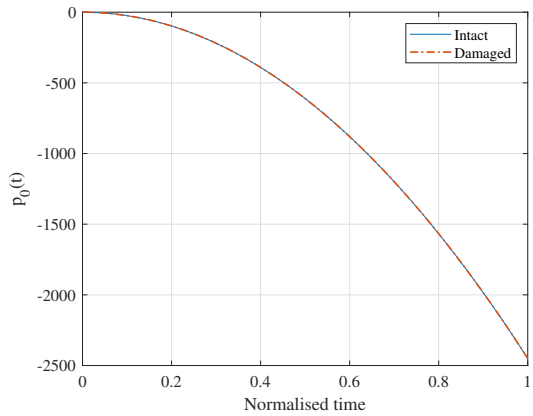

(b) $s = 10000$

Figure 6: The obtained value of $p_0(t)$ for both healthy and damaged structure when (a) $s = 1000$, (b) $s = 10000$.

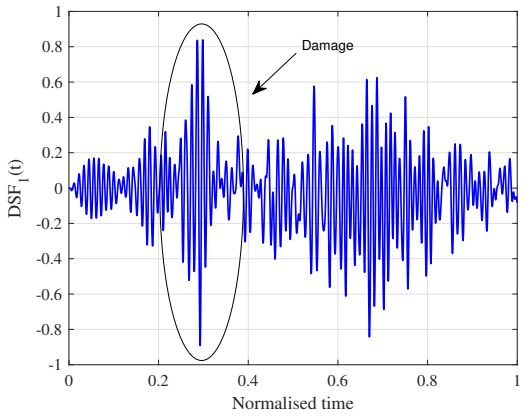

(a) DSF_1 ($s = 1000$)

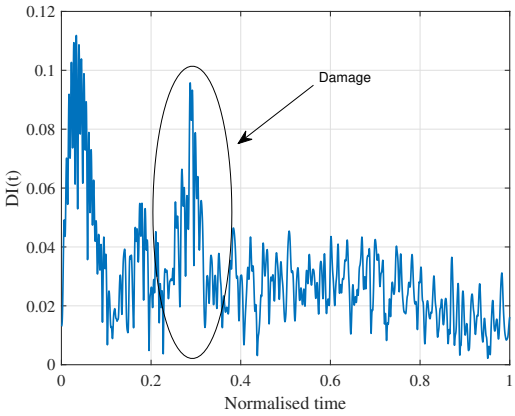

(b) DI ($s = 1000$)

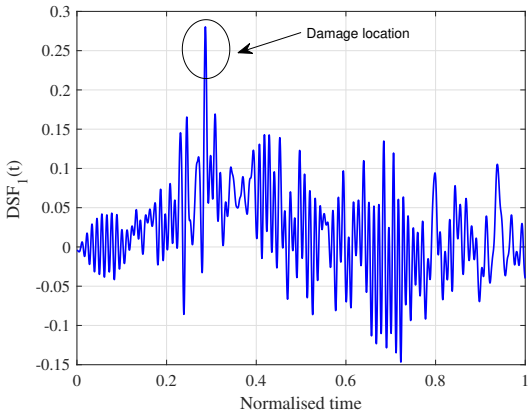

(c) DSF_1 ($s = 10000$)

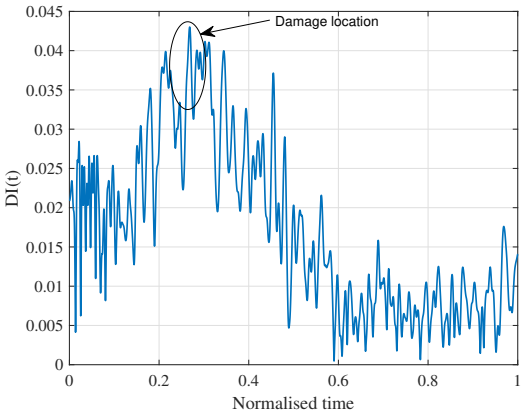

(d) DI ($s = 10000$)

Figure 7: Calculated DSF_1 and DI when a crack is present on the beam at normalised time $t = 0.2857$ when $s = 1000$ (a and b) and $s = 10000$ (c and d).

damaged from the intact case, with a smaller probability of a false alarm [34]. From these distributions $\mu \pm \sigma$ were evaluated and are shown in Table 3. The statistics show that the healthy and damaged results are separated by more than four standard deviations for DSF_1, but by less than two standard deviations for DI. Tthe proposed DSF_1 is therefore much more successful in separating the damaged and intact cases.

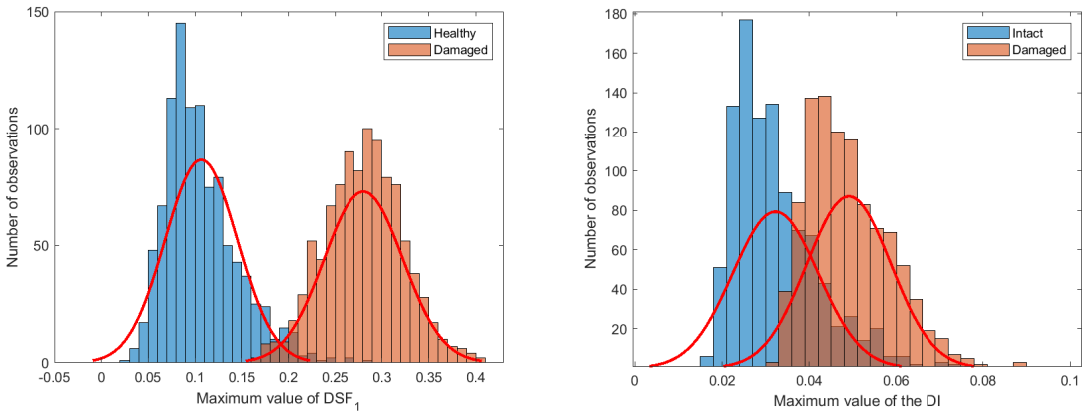

(a) Histogram of DSF_1 (b) Histogram of DI

Figure 8: Histograms of the maximum values of the (a) DSF_1 and (b) DI after 1000 Monte carlo simulations.

	DSF_1	**DI**
Healthy	0.1068 ± 0.0387	0.0323 ± 0.0098
Damaged	0.2803 ± 0.0421	0.0491 ± 0.0097
Damage location (m)	10.024 ± 0.006	12.481 ± 5.441

Table 3: Mean and standard deviation ($\mu \pm \sigma$) of DSF_1 and DI distributions shown in Figure 8 and of predicted damage locations shown in Figure 9.

Next the locations of the maximum DSF_1 and DI values are sought. Their box plots are shown in Figure 9 and $\mu \pm \sigma$ are again given in Table 3. The actual location is 10 m, so we see again that the proposed DSF_1 is significantly more successful in locating the damage.

Damage scenario D2 is now considered. Figure 10 shows the phase trajectory of the vibration of the beam mid-span using the noiseless (Figure 10a), noisy (Figure 10b), smoothed with $s = 1000$ (Figure 10c) and smoothed with $s = 10000$ (Figure 10d) normalised signals.

Again for this scenario, using $s = 1000$ results in a relatively large error for the damage detection. As evident from Figure 11b, it is hard to set a criterion for damage detection based on DI due to the large fluctuation of the DI when the mass starts traversing the beam. This effect has been also noted in the results presented in [17]. Although this fluctuation seems less critical at the beginning of the experiment when using DSF_1, some fluctuation of the DSF_1 can be noted slightly after the beam mid-span as evident from Figure 11a (as well as 7a).

However, once again the effect of these fluctuations is less significant when applying them to multiple damage cases with more aggressive smoothing of $s = 10000$. In this case a threshold is chosen for both DSF_1 and DI based on the Monte Carlo simulation strategy used earlier in this section. Accordingly, a threshold of 0.035 and 0.2 is chosen for DSF_1 and DI with the probability of detection of a 30% damage equal to about 97%. Although the thresholds are obtained for a damage severity of $\alpha = 0.3$, it can still be used to detect the second introduced crack with $\alpha = 0.2$ using the proposed DSF_1, as can be seen in Figure 11c. However, DI now does not detect the crack at a normalised time $t = 0.8286$ (Figure 11d). It is also evident from the figures that there are some false alarms in both cases. However, the effect of the false alarm is again less significant when using the proposed DSF.

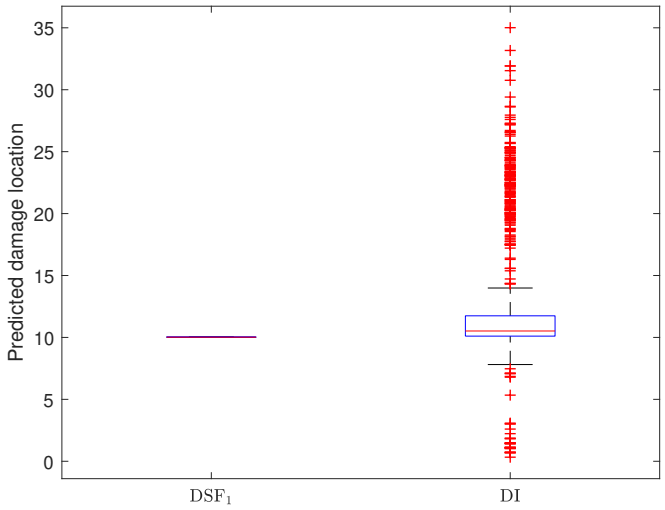

Figure 9: Box plot corresponding to the obtained location of the crack using DSF_1 and DI after 1000 Monte Carlo simulations.

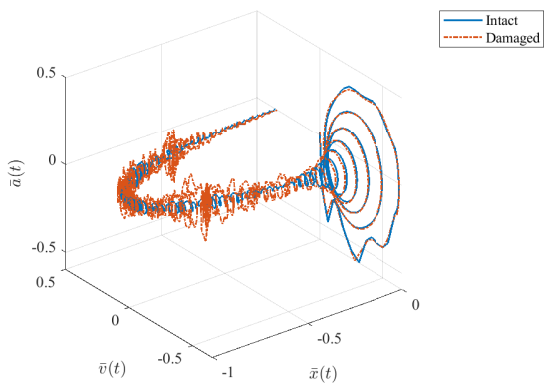

(a) Noiseless trajectories

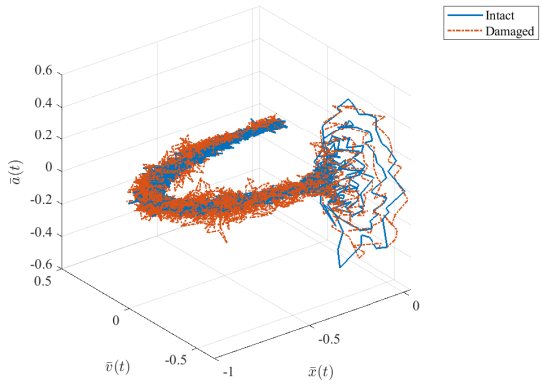

(b) Noisy trajectories

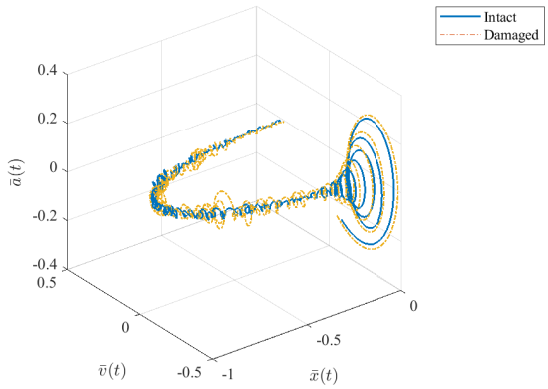

(c) Smoothed trajectories ($s = 1000$)

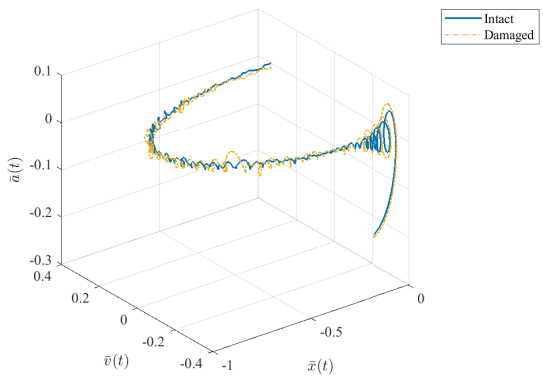

(d) Smoothed trajectories ($s = 10000$)

Figure 10: Phase trajectories of the intact and damaged beam subjected to a moving mass at its mid-span considering the road roughness effect, (a) noiseless, (b) noisy, and (c and d) smoothed.

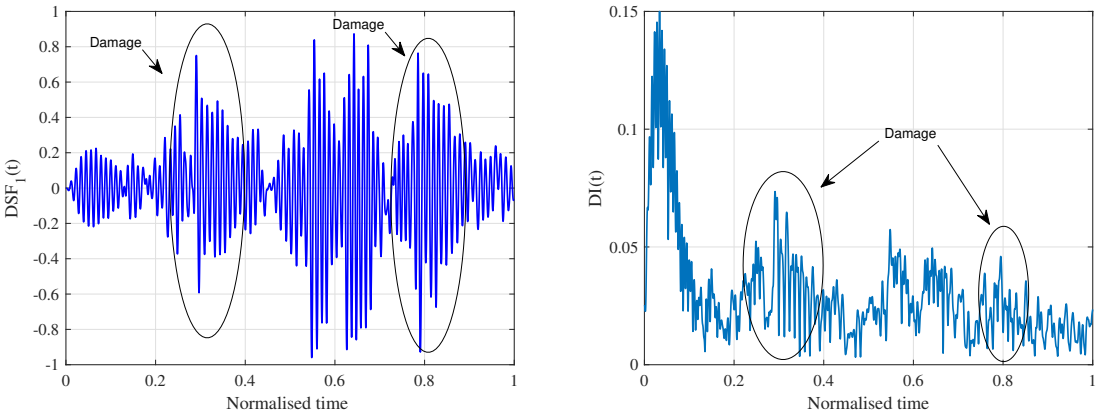

(a) DSF_1 (b) DI

(c) DSF_1 (d) DI

Figure 11: Calculated DSF_1 and DI when two cracks are present, one at normalised time $t = 0.2857$ with $\alpha = 0.3$ and the other at $t = 0.8286$ with $\alpha = 0.2$: (a and b) with $s = 1000$; (c and d) with $s = 10000$.

4.1.5. Damage detection using baseline dependent DSF_1 with a low-pass filter

In this section a low-pass filter is used as an alternative preconditioner to the cubic spline based smoothing. The three first natural frequencies of the intact beam are calculated to be 2.68, 10.70 and 24.08 Hz. Considering the sampling frequency of 100 Hz, a low-pass filter with a cutoff frequency of 3 Hz is used to mitigate the effect of the noise stemming from the measurement noise and the road roughness effects.

Figure 12 shows the single sided Fourier spectrum of the noiseless and noisy displacement (Figures 12a and 12b), velocity (Figures 12c and 12d) and acceleration (Figures 12e and 12f) time history of the beam mid-span for the duration of time when the mass traverses the beam. A spike representing the first natural frequency of the beam can be identified on all graphs except the noisy displacement. The Fourier spectra imply that the assumption that most of the information relies upon the first mode of the beam vibration is a reasonable one. Therefore, filtering out the higher frequency content should remove noise while retaining the valuable information, hence improve the detectability of the damage. This strategy has been reported to be useful for damage detection by others researchers [17, 35, 36, 37].

The phase trajectories of the beam for both single and multiple damage cases after using the low-pass filter are presented in Figure 13. It can be seen that the constructed phase trajectories for both damage scenarios is similar to the one obtained from using smoothing technique with $s = 1000$. This is also evident from the results of the damage detection presented in Figure 14. It is noted that no improvement in results was achieved by choosing a lower or higher cutoff frequency using either DSF_1 or DI. The damage detection results using a low-pass filter are not, therefore, as satisfactory as the ones obtained using the smoothing technique with $s = 10000$.

So far we have compared the results of the DSF_1 with DI to show the effectiveness of a Quaternion based technique for damage detection compared to DI. However, it is known that the baseline dependent techniques are less practical due to the challenges arising from the discrepancy between the velocity profile of the moving mass in two experiments. This becomes more challenging particularly when a large time has elapsed between two experiments exists. As such, the velocity profile of the former experiment may not be available to conduct the second experiment in a more controlled manner. Another issue arising from a large time separation comes from the environmental variations. Therefore, in the following section, the proposed DSF_1 is modified to obtain a baseline free DSF_2. We will show that the proposed DSF_2 is successful in detecting damage without using baseline information from the healthy structure.

4.2. A baseline-free damage detection method (DSF_2)

We now propose an alternative damage sensitive feature that does not rely on a baseline, denoted DSF_2 and based on the unit Quaternion.

Note that while the individual components of the previously defined Quaternion $q(t)$ in Section 4.1 have been normalised with respect to their maxima, the Quaternion itself at each time step $q(t)$ is not a unit Quaternion, hence we first normalize each sample to obtain

$$U_q(t) = \frac{q(t)}{||q(t)||}. \tag{32}$$

Its angular velocity, by Equation 20, is

$$\omega(t) = 2\,\dot{U}_q(t) \otimes U_q^*(t), \tag{33}$$

which according to Theorem 2 is a pure Quaternion, or a vector in $\mathbb{R}^3$. Then the baseline free DSF_2 is proposed as

$$\text{DSF}_2(t) = ||\omega^{(d)}(t)||\,||q^{(d)}(t)||. \tag{34}$$

The performance of DSF_2 is studied through numerical simulations in the sections to follow.

4.2.1. Results obtained using the baseline-free DSF_2

In this section, the proposed baseline-free DSF_2 is used to study simulated damage scenarios D1 and D2 defined in previous sections. In this section, the low-pass filter only is used for preconditioning of the simulated noisy signals prior to conducting damage detection.

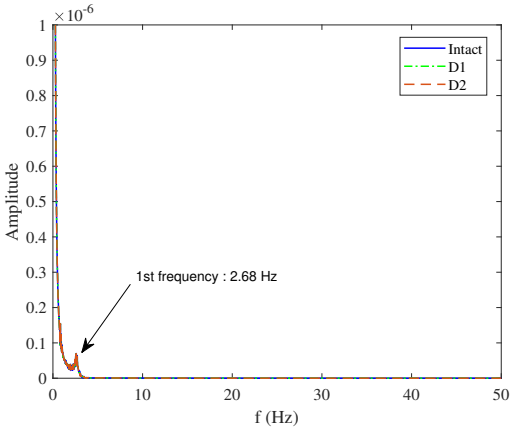

(a) noiseless displacement

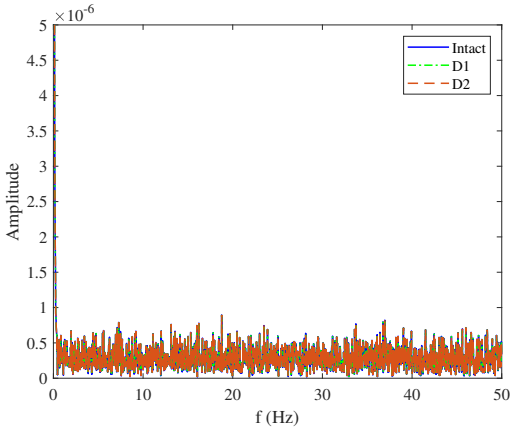

(b) noisy displacement (10%)

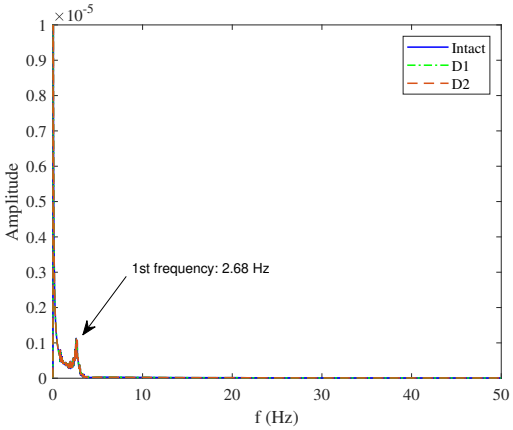

(c) noiseless velocity

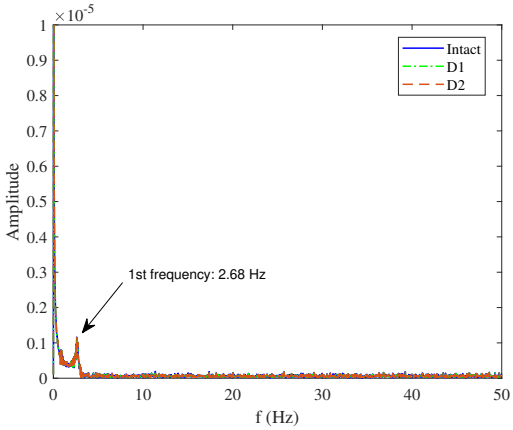

(d) noisy velocity (10%)

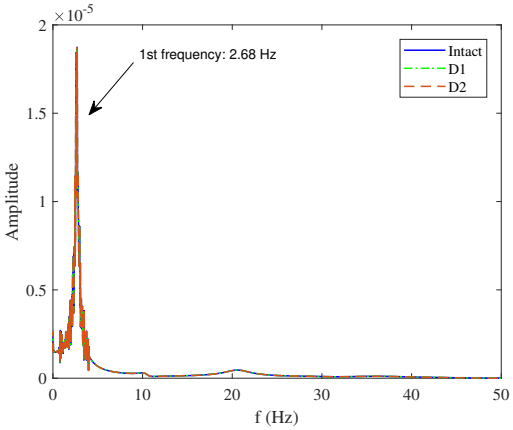

(e) noiseless acceleration

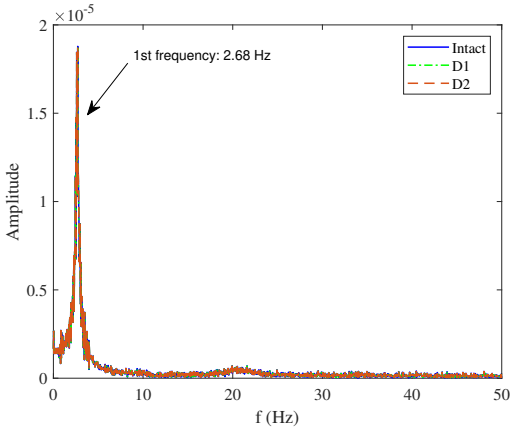

(f) noisy acceleration (10%)

Figure 12: Single sided Fourier spectrum of the noisy and noiseless displacement, velocity and acceleration of the intact and damaged beam mid-span subjected to the moving mass.

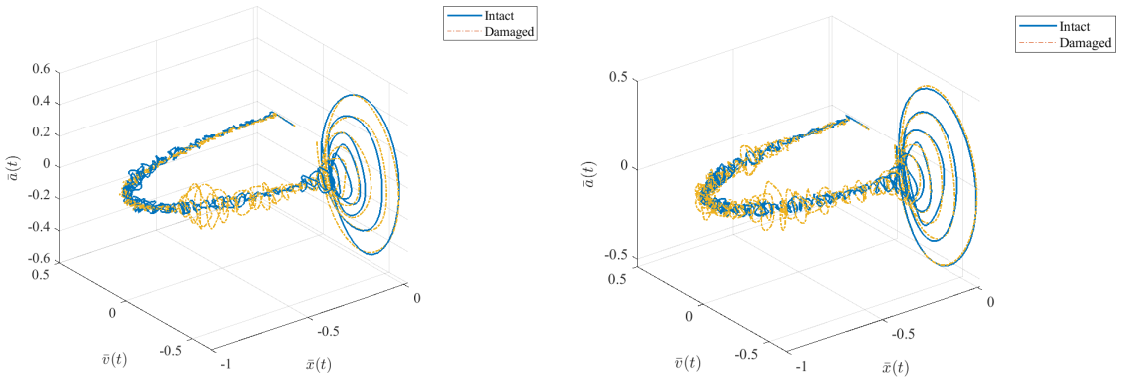

(a) Single damage (b) Multiple damage

Figure 13: Phase trajectory of the beam mid-span vibration after applying a low-pass filter with cut-off frequency of 3 Hz to the displacement, velocity and acceleration for the (a) single and (b) multiple damage scenario.

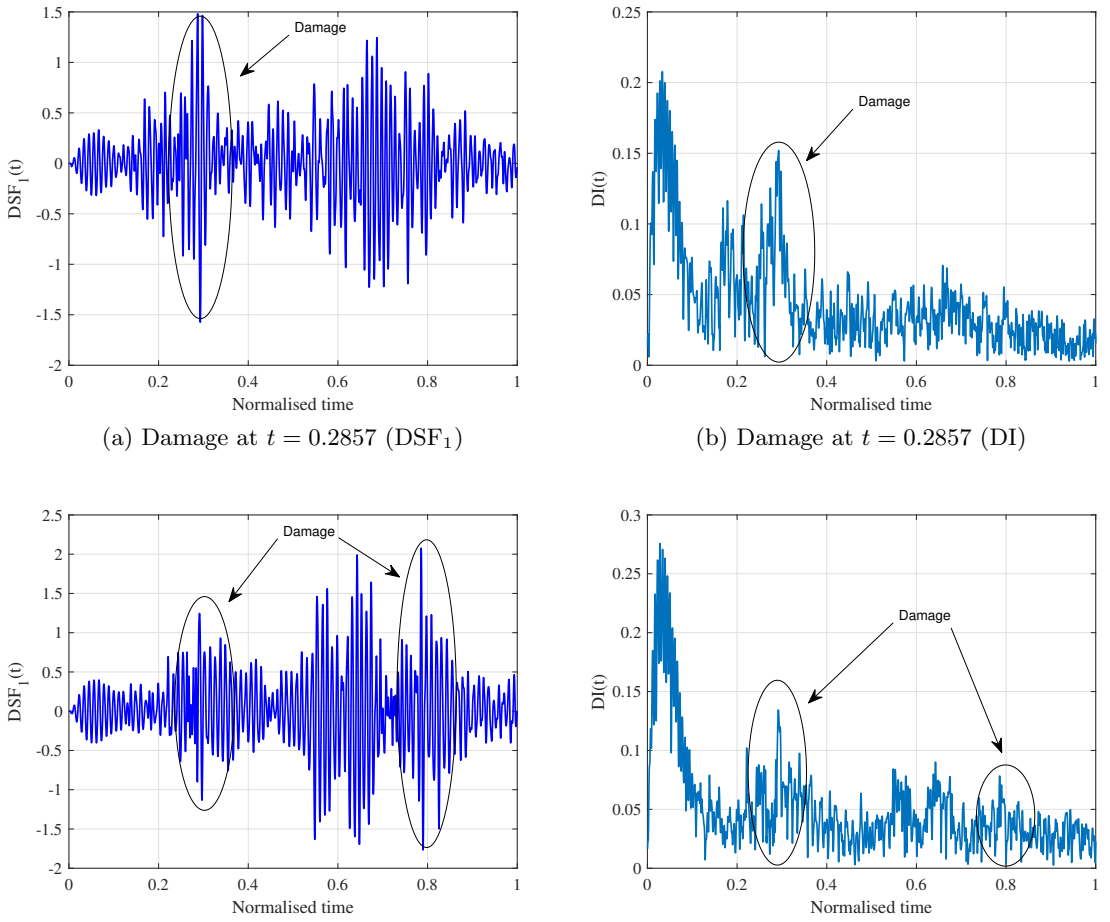

(a) Damage at $t = 0.2857$ (DSF_1) (b) Damage at $t = 0.2857$ (DI)

(c) Damage at $t = 0.2857$ and $t = 0.8286$ (DSF_1) (d) Damage at $t = 0.2857$ and $t = 0.8286$ (DI)

Figure 14: Damage detection results for DSF_1 (a and c) and DI (b and d) after prepossessing vibration signals using a low-pass filter for single and multiple damage scenarios.

First we present the norms of the angular velocity $||\omega^{(d)}(t)||$ and the constructed Quaternion $||q^{(d)}(t)||$ from the filtered normalised displacement $\bar{x}(t)$, velocity $\bar{v}(t)$, and acceleration $\bar{a}(t)$ obtained from damaged beam as presented in Figure 15. It is seen that damage is not easily detected in these signals. However by multiplying these element-wise to obtain the proposed DSF_2 one can see a greater resolution of the damage location, as evident in Figures 16a and 16b, which is successful in locating the damage, even though, in contrast to DSF_1 and DI, it is a baseline-free damage detection strategy.

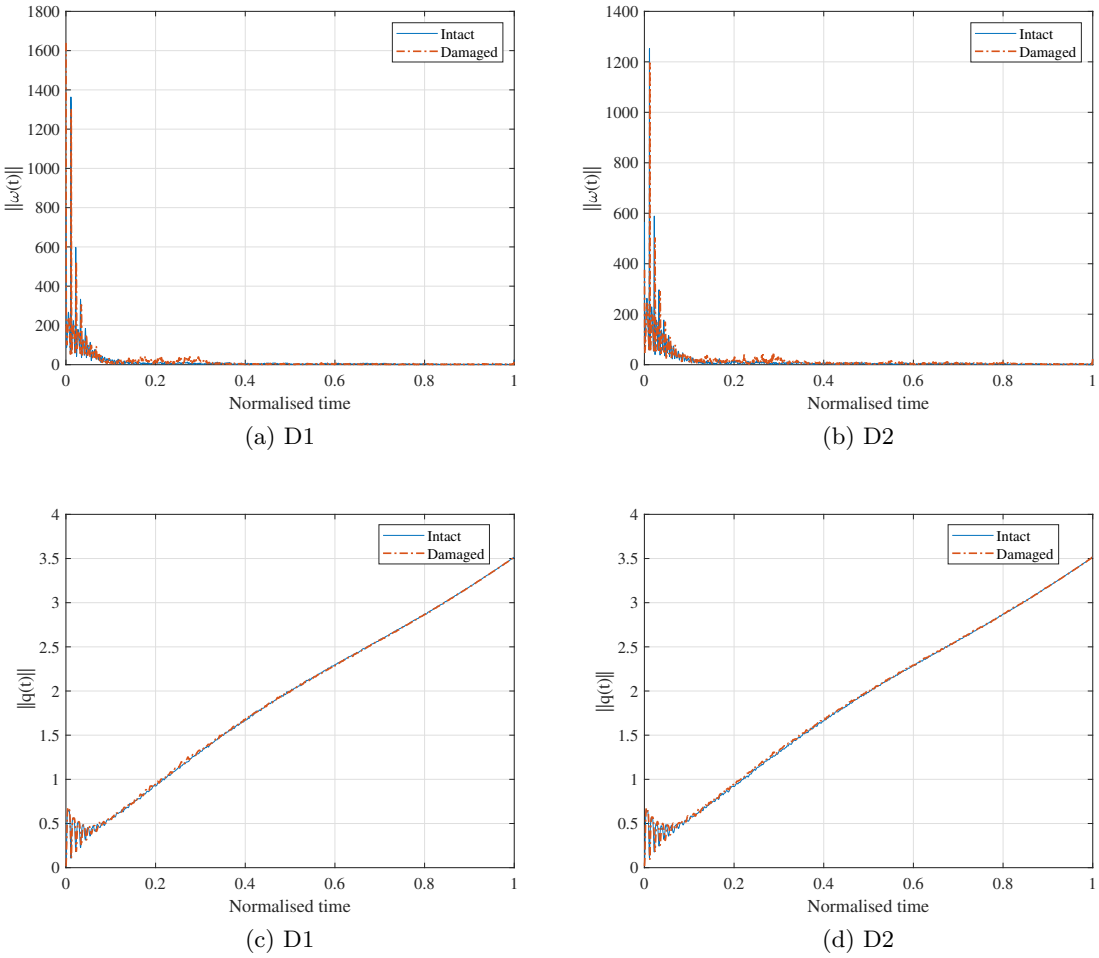

(a) D1 (b) D2

(c) D1 (d) D2

Figure 15: The graphs obtained for (a and b) $||\omega^{(d)}(t)||$ and (c and d) $||q^{(d)}(t)||$ after using the low-pass filter and normalising the signals.

For detection using DSF_2 it was noted that preconditioning using the smoothing technique causes loss of information about damage. This could be due mainly to the relatively large value of $||\omega^{(d)}(t)||$ $||q^{(d)}(t)||$ at the beginning of the experiment, which is disproportional to the rest of the graph as evident in Figure 16. This also makes damage detection within a normalised time range roughly between 0 and 0.1 challenging.

4.2.2. A damage detection strategy using DSF_2

Next, we propose to perform a test to confirm the location of the damage. This can be done by repeating the experiment in the opposite direction to the primary test. In other words, a mass now traverses the bridge from right to left [38]. Figure 17 depicts the proposed experiment.

Three different single damage scenarios are considered, in which a crack with $\alpha = 0.3$ exists at normalised times of respectively 0.2857, 0.5143, and 0.7429. Figures 18a, 18b, and 18c show the results of DSF_2^{LR} and DSF_2^{RL} for the left to right and right to left tests corresponding to each of the considered damage scenarios. In these figures, a normalised time of zero refers to the left end, regardless of the direction of the test.

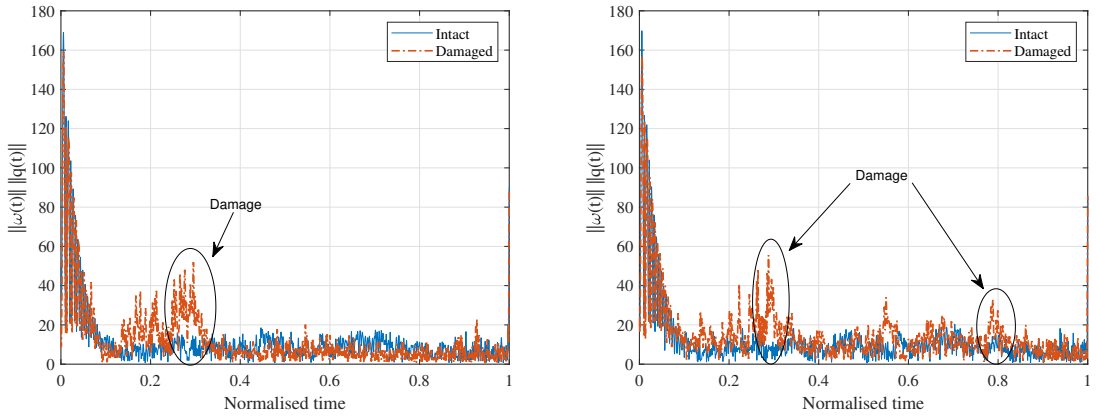

(a) DSF_2, D1 (b) DSF_2, D2

Figure 16: The obtained graphs for the proposed baseline free DSF_2 corresponding to damage scenarios D1 and D2.

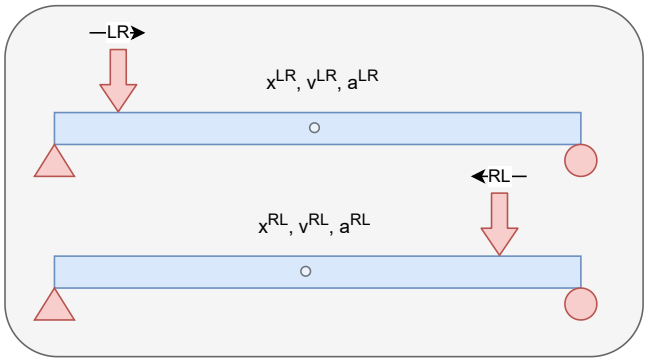

Figure 17: The experiment is repeated in both left-to-right (LR) and right-to-left (RL) directions and the displacement, acceleration and velocity signals are measured at the beam midspan.

As is evident from the graphs, it is still difficult to determine the location of the damage. One way to deal with this is to multiply the obtained DSF_2^{LR} and the flipped version of DSF_2^{RL} element-wise [39]. The element-wise multiplication will suppress the peak in locations other than the damage location and will enhance the peak obtained at the location of the damage [2]. Therefore, the procedure of the proposed strategy can be summarised as follows:

1. Conduct the experiment in both left to right (RL) and right to left (RL) directions and collect the displacement, velocity and acceleration time histories of the beam at its mid-span for both tests.
2. In the present numerical experiments, 10% noise is added to all the data using (29).
3. Apply a lowpass filter with the cutoff frequency 3 Hz to all the collected signals and normalise the signals using (25).
4. Construct the phase trajectory of the beam vibration at its midspan and evaluate DSF_2^{LR} and DSF_2^{RL}.
5. Perform the element-wise multiplication of the DSF_2^{LR} and flipped DSF_2^{RL} to enhance the peak at the location of the damage[3].

[2]Note that the peak related to other irregularities such as connection joints can also be enhanced through this process. However, a subsequent close inspection of the area can reveal whether the detected damage is genuine or otherwise.

[3]Note that even when the velocity profiles of the LR and RL experiments are not identical, the point to point comparison of the peaks is still possible by knowing the velocity profiles for both experiments. This may well not be, however, possible for the experiments conducted on the healthy and damaged structure when considerable time has elapsed between the two experiments.

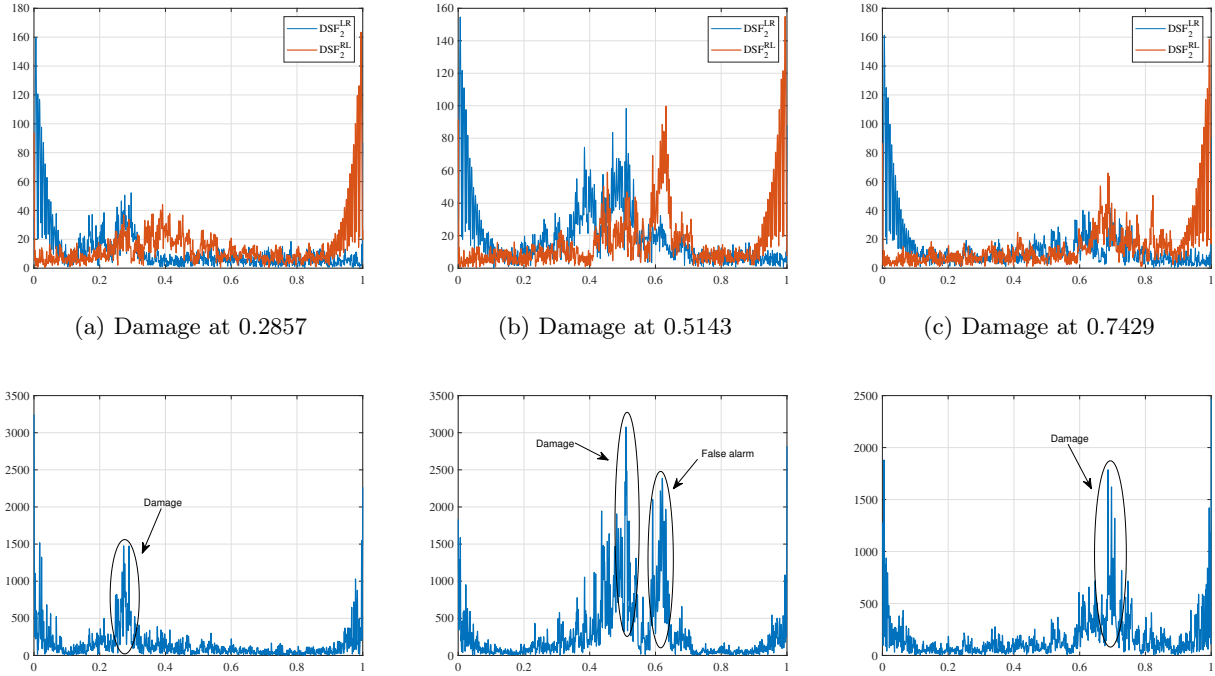

(a) Damage at 0.2857 (b) Damage at 0.5143 (c) Damage at 0.7429

(d) Damage at 0.2857 (e) Damage at 0.5143 (f) Damage at 0.7429

Figure 18: Results of damage detection for the test conducted in the left-right direction (DSF_2^{LR}) and right-left directions (DSF_2^{RL}) as well as the synchronised peaks at the location of damage when a crack with $\alpha = 0.3$ presents at normalised time 0.2857, 0.5143, and 0.7429.

Figures 18d, 18e, and 18f show the results of the peak synchronisation for each of the three damage scenarios considered. As can be seen in the figures, damage is successfully pinpointed as a peak. However, for the second scenario (damage at 0.5143), an extra peak is detected that cannot be attributed to any damage, and therefore, is indicated as a false alarm.

In order to examine the effectiveness of the proposed damage detection strategy for less severe damage cases, the same damage scenarios are considered with the relative crack depth now reduced to $\alpha = 0.1$.

Figure 19 shows the results that were obtained. As can be seen from the synchronised peaks of Figures 19d, 19e, and 19f, the damage detection still succeeds since a peak is apparent at the location of the crack in all scenarios. The next point that can be inferred from these figures is that while the amplitude of the peak has reduced in both damage scenarios of damage at 0.2857 and 0.7429, it, counter-intuitively, has increased at 0.5143 compared to the corresponding case of $\alpha = 0.3$. Regarding this observation, along with obtaining a false alarm for the case of damage at 0.5143 when $\alpha = 0.3$, we conclude the damage detection at the vicinity of the beam midspan using DSF_2 may be more challenging compared to other locations.

5. Conclusions and future work

In this paper, the phase trajectory of the vibration of a simply supported beam (bridge model) at its mid-span subjected to a moving sprung mass (vehicle model) is used for damage identification. To that end, two new damage sensitive features are proposed based on the Quaternion analysis technique, namely DSF_1 and DSF_2 which are respectively baseline-dependent and baseline-free methods, i.e. DSF_1 uses information from both the damaged and intact beam subjected to the same experiment, whereas DSF_2 only relies on information obtained from the damaged beam. The effects of both measurement noise and the road profile have been taken into account in all simulations. Results of damage detection using DSF_1 compared very favourably against DI, a similar damage index recently proposed in the literature that has been validated experimentally and shown to be successful [17].

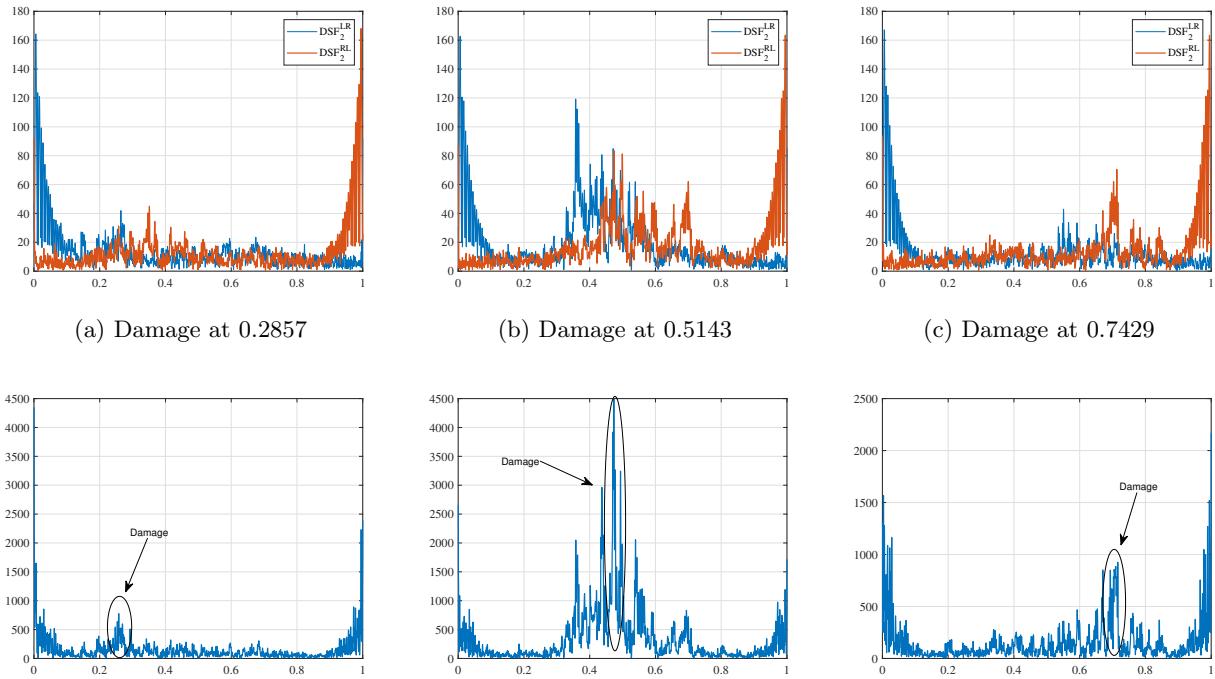

(a) Damage at 0.2857 (b) Damage at 0.5143 (c) Damage at 0.7429

(d) Damage at 0.2857 (e) Damage at 0.5143 (f) Damage at 0.7429

Figure 19: Results of damage detection for the test conducted in the left-right direction (DSF_2^{LR}) and right-left directions (DSF_2^{RL}) as well as the synchronised peaks at the location of damage when a crack with $\alpha = 0.1$ exists at normalised time 0.2857, 0.5143, and 0.7429.

The baseline-dependent DSF_1 was developed primarily to compare its results with the validated DI. However, the aim of this paper was ultimately to propose a baseline-free damage detection strategy, namely DSF_2, because in real applications considerable time is likely to have elapsed between experiments performed on the healthy and damaged structures. This will cause discrepancies between the results of the two experiments, for instance, from the moving mass velocity profile not being identical, the road being resurfaced, or environmental effects, and the differences between two experiment conditions may render the DSF_1 values obtained from both experiments incomparable.

The proposed baseline-free DSF_2 has been shown to be successful in detecting damage in the presence of realistic road roughness and a further 10% measurement noise. It was found that signal preconditioning was required for all the tested damage detection methods. Two techniques were applied in order to mitigate noise, a cubic spline based smoothing technique and a low-pass filter. Results show the former to be more successful for both DSF_1 and DI, while the latter was more successful for DSF_2. With optimal preconditioning the results show that the proposed DSF_1 outperforms DI, but that DSF_2 was able to detect damage without reference to a baseline.

It is noted that the detected peaks using either of the baseline dependent DSF_1 or DSF_2 do not always correspond to damage. This point has been shown through an experimental study in [17], in which a peak was detected at the location of a connecting plate. We therefore argue that a full scrutiny of the identified plausible defective area needs to be performed by engineers, to determine whether or not the detected damage is genuine. On the other hand, a peak can be repeated when multiple masses traverse the defective area, as shown experimentally in [17]. This effect can easily be monitored by knowing the distance between the car's axles and the speed of the moving vehicle.

Although some baseline-dependent strategies have so far been developed by researchers (for example [16]), the challenge arising from the discrepancy between the experimental results obtained from the healthy and damaged structure still needs to be addressed in these techniques. The results obtained using the proposed DSF_2 are therefore promising. However, it is important to note that the results of this paper are considered as a foundation for future research in which experimental studies must be conducted for further confirmation. It is apparent that damage detection on a sim-

ply supported beam using a moving mass experiment and considering the road roughness effect is a challenging task.

In the constructed Quaternion $q(t)$, time (t) is considered as the scalar part. However, other possible scalar quantities (such as the norm of the vector part of the Quaternion) could be used and tested for likely improvement of the proposed DSFs, which could be the subject of future work. It is also recommended that other more advanced time domain signal decomposition techniques such as VMD could be trialled to de-noise the signal more properly while still preserving the useful information about damage, which may bring about further improvements to detection.

References

[1] Y. An, E. Chatzi, S.-H. Sim, S. Laflamme, B. Blachowski, J. Ou, Recent progress and future trends on damage identification methods for bridge structures, Structural Control and Health Monitoring 26 (10) (2019) e2416.

[2] V. Pakrashi, A. O'Connor, B. Basu, A bridge-vehicle interaction based experimental investigation of damage evolution, Structural Health Monitoring 9 (4) (2010) 285–296.

[3] Y. Yang, J. P. Yang, State-of-the-art review on modal identification and damage detection of bridges by moving test vehicles, International Journal of Structural Stability and Dynamics 18 (02) (2018) 1850025.

[4] W.-Y. He, W.-X. Ren, S. Zhu, Damage detection of beam structures using quasi-static moving load induced displacement response, Engineering Structures 145 (2017) 70–82.

[5] M. Link, M. Weiland, Damage identification by multi-model updating in the modal and in the time domain, Mechanical Systems and Signal Processing 23 (6) (2009) 1734–1746.

[6] E. J. OBrien, A. Malekjafarian, A mode shape-based damage detection approach using laser measurement from a vehicle crossing a simply supported bridge, Structural Control and Health Monitoring 23 (10) (2016) 1273–1286.

[7] N. E. Huang, Z. Shen, S. R. Long, M. C. Wu, H. H. Shih, Q. Zheng, N.-C. Yen, C. C. Tung, H. H. Liu, The empirical mode decomposition and the hilbert spectrum for nonlinear and non-stationary time series analysis, Proceedings of the Royal Society of London. Series A: Mathematical, Physical and Engineering Sciences 454 (1971) (1998) 903–995.

[8] K. Dragomiretskiy, D. Zosso, Variational mode decomposition, IEEE transactions on signal processing 62 (3) (2013) 531–544.

[9] Y. An, B. Spencer, J. Ou, A test method for damage diagnosis of suspension bridge suspender cables, Computer-Aided Civil and Infrastructure Engineering 30 (10) (2015) 771–784. doi:10.1111/mice.12144.

[10] A. Khorram, F. Bakhtiari-Nejad, M. Rezaeian, Comparison studies between two wavelet based crack detection methods of a beam subjected to a moving load, International Journal of Engineering Science 51 (2012) 204–215.

[11] W.-Y. He, S. Zhu, Moving load-induced response of damaged beam and its application in damage localization, Journal of Vibration and Control 22 (16) (2016) 3601–3617.

[12] N. Roveri, A. Carcaterra, Damage detection in structures under traveling loads by hilbert–huang transform, Mechanical Systems and Signal Processing 28 (2012) 128–144.

[13] J. Meredith, A. González, D. Hester, Empirical mode decomposition of the acceleration response of a prismatic beam subject to a moving load to identify multiple damage locations, Shock and Vibration 19 (5) (2012) 845–856.

[14] A. Kunwar, R. Jha, M. Whelan, K. Janoyan, Damage detection in an experimental bridge model using hilbert–huang transform of transient vibrations, Structural Control and Health Monitoring 20 (1) (2013) 1–15.

[15] F. Meng, B. Mokrani, D. Alaluf, J. Yu, A. Preumont, Damage detection in active suspension bridges: An experimental investigation, Sensors 18 (9) (2018) 3002.

[16] E. J. OBrien, A. Malekjafarian, A. González, Application of empirical mode decomposition to drive-by bridge damage detection, European Journal of Mechanics-A/Solids 61 (2017) 151–163.

[17] W. Zhang, J. Li, H. Hao, H. Ma, Damage detection in bridge structures under moving loads with phase trajectory change of multi-type vibration measurements, Mechanical Systems and Signal Processing 87 (2017) 410–425.

[18] Z. Sun, T. Nagayama, M. Nishio, Y. Fujino, Investigation on a curvature-based damage detection method using displacement under moving vehicle, Structural Control and Health Monitoring 25 (1) (2018) e2044.

[19] Q. Yang, J. Liu, B. Sun, C. Liang, Damage localization for beam structure by moving load, Advances in Mechanical Engineering 9 (3) (2017) 1687814017695956.

[20] Y. Yang, C. Lin, Vehicle–bridge interaction dynamics and potential applications, Journal of sound and vibration 284 (1-2) (2005) 205–226.

[21] L. Vu-Quoc, M. Olsson, A computational procedure for interaction of high-speed vehicles on flexible structures without assuming known vehicle nominal motion, Computer Methods in Applied Mechanics and Engineering 76 (3) (1989) 207–244.

[22] S.-H. Ju, H.-T. Lin, C.-C. Hsueh, S.-L. Wang, A simple finite element model for vibration analyses induced by moving vehicles, International journal for numerical methods in engineering 68 (12) (2006) 1232–1256.

[23] H. Ouyang, J. E. Mottershead, A numerical–analytical combined method for vibration of a beam excited by a moving flexible body, International Journal for Numerical Methods in Engineering 72 (10) (2007) 1181–1191.

[24] M. Agostinacchio, D. Ciampa, S. Olita, The vibrations induced by surface irregularities in road pavements—a Matlab® approach, European Transport Research Review 6 (3) (2014) 267–275.

[25] B. Zhang, Y. Qian, Y. Wu, Y. Yang, An effective means for damage detection of bridges using the contact-point response of a moving test vehicle, Journal of Sound and Vibration 419 (2018) 158–172.

[26] M. R. Heller, Automotive Simulation'91: A Simulation Model for Passive Suspension Ride Performance Optimization, Proceedings of the 3rd European Cars/Trucks, Simulation Symposium Schliersee, Germany, October 1991, Springer Science & Business Media, 2012.

[27] A. Pandey, M. Biswas, M. Samman, Damage detection from changes in curvature mode shapes, Journal of Sound and Vibration 145 (2) (1991) 321–332.

[28] J. Lee, J. Kim, C. B. Yun, J. Yi, J. Shim, Health-monitoring method for bridges under ordinary traffic loadings, Journal of Sound and Vibration 257 (2) (2002) 247–264.

[29] H. Tada, P. Paris, G. Irwin, The analysis of cracks handbook, New York: ASME Press 2 (2000) 1.

[30] W. R. Hamilton, On quaternions; or on a new system of imagniaries in algebra, London, Edinburgh, and Dublin Philosophical Magazine and Journal of Science 25(3) (1844) 489–495.

[31] Y.-B. Jia, Quaternions and rotations, Com S 477 (577) (2008) 15.

[32] D. Garcia, Robust smoothing of gridded data in one and higher dimensions with missing values, Computational statistics & data analysis 54 (4) (2010) 1167–1178.

[33] S. Oller, A. H. Barbat, Moment–curvature damage model for bridges subjected to seismic loads, Computer Methods in Applied Mechanics and Engineering 195 (33-36) (2006) 4490–4511.

[34] J. D. Gibson, J. L. Melsa, Introduction to nonparametric detection with applications, Chapter (2); Basic Detection Theory, Vol. 119, Academic Press, 1976.

[35] E. Douka, S. Loutridis, A. Trochidis, Crack identification in beams using wavelet analysis, International Journal of Solids and Structures 40 (13-14) (2003) 3557–3569.

[36] J.-C. Hong, Y. Kim, H. Lee, Y. Lee, Damage detection using the lipschitz exponent estimated by the wavelet transform: applications to vibration modes of a beam, International journal of solids and structures 39 (7) (2002) 1803–1816.

[37] W. Zhang, Z. Wang, H. Ma, Crack identification in stepped cantilever beam combining wavelet analysis with transform matrix, Acta Mechanica Solida Sinica 22 (4) (2009) 360–368.

[38] M. Mousavi, D. Holloway, J. Olivier, Using a moving load to simultaneously detect location and severity of damage in a simply supported beam, Journal of Vibration and Control 25 (15) (2019) 2108–2123.

[39] M. Mousavi, D. Holloway, J. Olivier, A. H. Gandomi, Beam damage detection using synchronisation of peaks in instantaneous frequency and amplitude of vibration data, Measurement 168 108297.